The Transiting Multi-planet System HD15337: Two Nearly Equal-mass Planets Straddling the Radius Gap

Davide Gandolfi[1] , Luca Fossati[2] , John H. Livingston[3] , Keivan G. Stassun[4,5] , Sascha Grziwa[6] , Oscar Barragán[7], Malcolm Fridlund[8,9] , Daria Kubyshkina[2], Carina M. Persson[8], Fei Dai[10,11], Kristine W. F. Lam[12], Simon Albrecht[13], Natalie Batalha[14], Paul G. Beck[15,16], Anders Bo Justesen[13], Juan Cabrera[17] , Scott Cartwright[18], William D. Cochran[19] , Szilard Csizmadia[17], Misty D. Davies[20], Hans J. Deeg[15,16] , Philipp Eigmüller[17], Michael Endl[19] , Anders Erikson[17], Massimiliano Esposito[21], Rafael A. García[22], Robert Goeke[10], Lucía González-Cuesta[15,16], Eike W. Guenther[21], Artie P. Hatzes[21], Diego Hidalgo[15], Teruyuki Hirano[23] , Maria Hjorth[13], Petr Kabath[24] , Emil Knudstrup[13], Judith Korth[6], Jie Li[25], Rafael Luque[15,16], Savita Mathur[15,16], Pilar Montañes Rodríguez[15,16], Norio Narita[3,15,26,27,28] , David Nespral[15,16], Prajwal Niraula[29] , Grzegorz Nowak[15,16] , Enric Palle[15,16], Martin Pätzold[6], Jorge Prieto-Arranz[15,16], Heike Rauer[12,17,30], Seth Redfield[31] , Ignasi Ribas[32,33] , Marek Skarka[24,34] , Alexis M. S. Smith[17], Pamela Rowden[35], Guillermo Torres[36], Vincent Van Eylen[11], and Michael L. Vezie[10]

[1] Dipartimento di Fisica, Università degli Studi di Torino, via Pietro Giuria 1, I-10125, Torino, Italy; davide.gandolfi@unito.it
[2] Space Research Institute, Austrian Academy of Sciences, Schmiedlstrasse 6, A-8041 Graz, Austria
[3] Department of Astronomy, University of Tokyo, 7-3-1 Hongo, Bunkyo-ku, Tokyo 113-0033, Japan
[4] Vanderbilt University, Department of Physics & Astronomy, 6301 Stevenson Center Lane, Nashville, TN 37235, US
[5] Fisk University, Department of Physics, 1000 17th Avenue North, Nashville, TN 37208, US
[6] Rheinisches Institut für Umweltforschung an der Universität zu Köln, Aachener Strasse 209, D-50931 Köln, Germany
[7] Oxford Astrophysics, Department of Physics, University of Oxford, Denys Wilkinson Building, Keble Road, Oxford OX1 3RH, UK
[8] Department of Space, Earth and Environment, Chalmers University of Technology, Onsala Space Observatory, SE-439 92 Onsala, Sweden
[9] Leiden Observatory, University of Leiden, PO Box 9513, 2300 RA, Leiden, The Netherlands
[10] Department of Physics and Kavli Institute for Astrophysics and Space Research, MIT, Cambridge, MA 02139, USA
[11] Department of Astrophysical Sciences, Princeton University, 4 Ivy Lane, Princeton, NJ 08544, USA
[12] Center for Astronomy and Astrophysics, TU Berlin, Hardenbergstr. 36, D-10623 Berlin, Germany
[13] Stellar Astrophysics Centre, Dep. of Physics and Astronomy, Aarhus University, Ny Munkegade 120, DK-8000 Aarhus C, Denmark
[14] Department of Astronomy and Astrophysics, University of California, Santa Cruz, CA 95064, USA
[15] Instituto de Astrofísica de Canarias, C/ Vía Láctea s/n, E-38205 La Laguna, Spain
[16] Departamento de Astrofísica, Universidad de La Laguna, E-38206 La Laguna, Spain
[17] Institute of Planetary Research, German Aerospace Center, Rutherfordstrasse 2, D-12489 Berlin, Germany
[18] Proto-Logic LLC, 1718 Euclid Street NW, Washington, DC 20009, USA
[19] Department of Astronomy and McDonald Observatory, University of Texas at Austin, 2515 Speedway, Stop C1400, Austin, TX 78712, USA
[20] NASA Ames Research Center, Moffett Field, CA 94035, USA
[21] Thüringer Landessternwarte Tautenburg, Sternwarte 5, D-07778 Tautenberg, Germany
[22] Laboratoire AIM, CEA/DSM—CNRS—Univ. Paris Diderot - IRFU/SAp, Centre de Saclay, F-91191 Gif-sur-Yvette, France
[23] Department of Earth and Planetary Sciences, Tokyo Institute of Technology, 2-12-1 Ookayama, Meguro-ku, Tokyo 152-8551, Japan
[24] Astronomical Institute, Czech Academy of Sciences, Fričova 298, 25165, Ondřejov, Czech Republic
[25] Aerospace Computing Inc./NASA Ames Research Center, Moffett Field, CA 94035, USA
[26] Astrobiology Center, NINS, 2-21-1 Osawa, Mitaka, Tokyo 181-8588, Japan
[27] National Astronomical Observatory of Japan, NINS, 2-21-1 Osawa, Mitaka, Tokyo 181-8588, Japan
[28] JST, PRESTO, 7-3-1 Hongo, Bunkyo-ku, Tokyo 113-0033, Japan
[29] Department of Earth, Atmospheric and Planetary Sciences, Massachusetts Institute of Technology, Cambridge, MA 02139, USA
[30] Institute of Geological Sciences, FU Berlin, Malteserstr. 74-100, D-12249 Berlin
[31] Astronomy Department and Van Vleck Observatory, Wesleyan University, Middletown, CT 06459, USA
[32] Institut de Ciències de l'Espai (ICE, CSIC), Campus UAB, C/ de Can Magrans s/n, E-08193 Bellaterra, Spain
[33] Institut d'Estudis Espacials de Catalunya (IEEC), C/ Gran Capità 2-4, E-08034 Barcelona, Spain
[34] Department of Theoretical Physics and Astrophysics, Masaryk University, Kotlářská 2, 61137 Brno, Czech Republic
[35] School of Physical Sciences, The Open University, Walton Hall, Milton Keynes MK7 6AA, UK
[36] Center for Astrophysics | Harvard & Smithsonian, 60 Garden Street, Cambridge, MA 02138, USA

Abstract

We report the discovery of a super-Earth and a sub-Neptune transiting the star HD 15337 (TOI-402, TIC 120896927), a bright ($V = 9$) K1 dwarf observed by the *Transiting Exoplanet Survey Satellite* (*TESS*) in Sectors 3 and 4. We combine the *TESS* photometry with archival High Accuracy Radial velocity Planet Searcher spectra to confirm the planetary nature of the transit signals and derive the masses of the two transiting planets. With an orbital period of 4.8 days, a mass of $7.51^{+1.09}_{-1.01}\,M_\oplus$ and a radius of $1.64 \pm 0.06\,R_\oplus$, HD 15337 b joins the growing group of short-period super-Earths known to have a rocky terrestrial composition. The sub-Neptune HD 15337 c has an orbital period of 17.2 days, a mass of $8.11^{+1.82}_{-1.69}\,M_\oplus$, and a radius of $2.39 \pm 0.12\,R_\oplus$, suggesting that the planet might be surrounded by a thick atmospheric envelope. The two planets have similar masses and lie on opposite sides of the radius gap, and are thus an excellent testbed for planet formation and evolution theories. Assuming that HD 15337 c hosts a hydrogen-dominated envelope, we employ a recently developed planet atmospheric evolution algorithm in a Bayesian framework to estimate the history of the high-energy (extreme ultraviolet and X-ray) emission of the host star. We find that at an age of 150 Myr, the star possessed on average between 3.7 and 127 times the high-energy luminosity of the current Sun.

1. Introduction

Successfully launched in 2018 April, NASA's *Transiting Exoplanet Survey Satellite* (*TESS*) is making a significant step forward in understanding the diversity of exoplanets, especially of super-Earths ($R_p = 1$–$2\,R_\oplus$) and sub-Neptunes ($R_p = 2$–$4\,R_\oplus$). *TESS* is performing an all-sky photometric search for planets transiting bright stars ($6 < V < 11$), so that detailed characterizations of the planets and their atmospheres can be performed (Ricker et al. 2015). The survey is broken up into 26 sectors— each sector being observed for ∼28 days and consisting of four cameras with a combined field of view of $24° \times 96°$. Candidate alerts and full-frame images are released every month. As of 2019 March, *TESS* has already announced the discovery of about a dozen transiting planets (see, e.g., Gandolfi et al. 2018; Huang et al. 2018; Jones et al. 2018; Esposito et al. 2019; Nielsen et al. 2019; Quinn et al. 2019; Trifonov et al. 2019).

TESS has already led to the detection of "golden" systems amenable to in-depth characterization of planetary atmospheres, such as π Men, which is a bright ($V = 5.65$) star hosting a transiting super-Earth with a bulk density that is consistent with either a primary, hydrogen-dominated atmosphere, or a secondary, probably CO_2/H_2O-dominated, atmosphere (Gandolfi et al. 2018; Huang et al. 2018). The discovery of such systems is central for studying planetary atmospheres via multi-wavelength transmission spectroscopy, and for constraining the evolution models of planetary atmospheres.

TESS also enables the discovery of multi-planet systems for which both mass and radius can be precisely measured. Because such planets orbit the same star, differences in mean density and atmospheric structure among planets belonging to the same system can be ascribed mainly to differences in planetary mass and orbital separation (see, e.g., Guenther et al. 2017; Prieto-Arranz et al. 2018). This greatly simplifies modeling of their past evolution history, thus constraining how these planets formed (Alibert et al. 2005; Alibert & Benz 2017). In this respect, even more significant are multi-planet systems in which two or more planets have similar masses, as differences in radii would most likely be due to the different orbital separations.

In this Letter we report the discovery of two small planets transiting the bright ($V = 9$) star HD 15337 (Table 1), a K1 dwarf observed by *TESS* in Sectors 3 and 4. We combined the *TESS* photometry with archival High Accuracy Radial velocity Planet Searcher (HARPS) radial velocities (RVs) to confirm the planetary nature of the transit signals and derive the masses of the two planets. This Letter is organized as follows. In Section 2, we describe the *TESS* photometry and the detection of the transit signals. In Section 3, we present the archival HARPS spectra. The properties of the host star are reported in Section 4. We present the frequency analysis of the HARPS RVs in Section 5 and the data modeling in Section 6. Results, discussions, and a summary are given in Section 7.

2. *TESS* Photometry

HD 15337 (TIC 120896927) was observed by *TESS* Camera #2 in Sectors 3 and 4 (charge-coupled devices #3 and #4,

respectively) from 2018 September 20 to November 15, and will not be observed further during the nominal two-year *TESS* mission. Photometry was interrupted when the satellite was re-pointed for data downlink, from $\mathrm{BJD_{TDB}} = 2458395.4$ to $\mathrm{BJD_{TDB}} = 2458396.6$ in Sector 3, and from $\mathrm{BJD_{TDB}} = 2458423.5$ to $\mathrm{BJD_{TDB}} = 2458424.6$ in Sector 4. There is an additional data gap in Sector 4 from $\mathrm{BJD_{TDB}} = 2458418.5$ to $\mathrm{BJD_{TDB}} = 2458421.2$, which was caused by an interruption in communications between the instrument and spacecraft.

TESS objects of interest (TOIs) are announced publicly via the *TESS* data alerts web portal[37] at the Massachusetts Institute of Technology. TOIs 402.01 (HD 15337 b) and 402.02 (HD 15337 c) were announced on 2019 January 16 and 31, respectively, in association with the HD 15337 photometry. The *TESS* pixel data and light curves produced by the Science Processing Operations Center (SPOC; Jenkins et al. 2016) at NASA Ames Research Center were subsequently made publicly available via the Mikulski Archive for Space Telescopes (MAST).[38] We iteratively searched the SPOC light curves for transit signals using the Box-least-squares algorithm (BLS; Kovács et al. 2002), after fitting and removing stellar variability using a cubic spline with knots every 1.0 day. We recovered two signals corresponding to the TOIs, but no other significant signals were detected. We also tried removing variability using the wavelet-based filter routines `VARLET` and `PHALET`, but it did not change the BLS results; we are thus confident that the two signals are robustly detected and are not the result of data artifacts resulting from the choice of variability model or residual instrumental systematic signals.

The SPOC light curves are produced using automatically selected optimal photometric apertures. We also produced light curves from the *TESS* pixel data using a series of apertures (Gandolfi et al. 2018; Esposito et al. 2019), and found that apertures larger than the SPOC aperture shown in Figure 1 minimized the 6.5 hr combined differential photometric precision noise metric (Christiansen et al. 2012). However, the transit signals recovered from these light curves were slightly less significant, which we attributed to the improvement in light curve quality afforded by the Presearch Data Conditioning (Smith et al. 2012; Stumpe et al. 2012) pipeline used by the SPOC, which corrects for common-mode systematic noise; for this reason, we opted to analyze the SPOC light curves for the remainder of the analysis in this Letter.

To investigate the possibility of diluting flux from stars other than HD 15337, we visually inspected archival images and compared *Gaia* DR2 (Gaia Collaboration et al. 2018) source positions with the SPOC photometric apertures. We used the coordinates of HD 15337 from the *TESS* Input Catalog[39] (Stassun et al. 2018b) to retrieve *Gaia* DR2 sources using a search radius of 3′. In an archival image taken in 1955 from the First Palomar Sky Survey (POSS1-E)[40], HD 15337 is offset from its current position by ∼14″ due to proper motion, but this

---

Table 1
Main Identifiers, Coordinates, Proper Motion, Parallax, Distance, and Optical and Infrared Magnitudes of HD 15337

Parameter	Value	Source
Main Identifiers		
HD	15337	
HIP	11433	*Hipparcos*
TIC	120896927	TIC[a]
TOI	402	*TESS* Alerts
Gaia DR2	5068777809824976256	*Gaia* DR2[b]
Equatorial Coordinates		
R.A. (J2000.0)	$02^h\ 27^m\ 28\overset{s}{.}3781$	*Gaia* DR2[b]
Decl. (J2000.0)	$-27°\ 38'\ 06\overset{''}{.}7417$	*Gaia* DR2[b]
Proper Motion, Parallax, and Distance		
$\mu_\alpha \cos\delta$ (mas yr^{-1})	-73.590 ± 0.057	*Gaia* DR2[b]
μ_δ (mas yr^{-1})	-211.614 ± 0.082	*Gaia* DR2[b]
Parallax (mas)	22.285 ± 0.035	*Gaia* DR2[b]
Distance (pc)	44.874 ± 0.070	*Gaia* DR2[b]
Magnitudes		
B_T	10.170 ± 0.027	*Tycho*-2[c]
V_T	9.184 ± 0.018	*Tycho*-2[c]
B	10.009 ± 0.090	APASS[d]
V	9.096 ± 0.017	APASS[d]
g	9.852 ± 0.493	APASS[d]
r	8.847 ± 0.016	APASS[d]
i	8.655 ± 0.054	APASS[d]
u	11.756 ± 0.075	Strömgren[e]
v	10.526 ± 0.046	Strömgren[e]
b	9.598 ± 0.032	Strömgren[e]
y	9.088 ± 0.030	Strömgren[e]
G	8.8560 ± 0.0002	*Gaia* DR2[b]
G_{BP}	9.3194 ± 0.0011	*Gaia* DR2[b]
G_{RP}	8.2708 ± 0.0016	*Gaia* DR2[b]
J	7.553 ± 0.019	2MASS[f]
H	7.215 ± 0.034	2MASS[f]
K_s	7.044 ± 0.018	2MASS[f]
$W1(3.35\ \mu m)$	6.918 ± 0.054	ALLWISE[g]
$W2(4.6\ \mu m)$	7.048 ± 0.020	ALLWISE[g]
$W3(11.6\ \mu m)$	7.015 ± 0.017	ALLWISE[g]
$W4(22.1\ \mu m)$	6.916 ± 0.072	ALLWISE[g]

Notes.
[a] *TESS* Input Catalog (TIC; Stassun et al. 2018b).
[b] *Gaia* Data Release 2 (DR2; Gaia Collaboration et al. 2018).
[c] *Tycho*-2 catalog (Høg et al. 2000).
[d] AAVSO Photometric All-Sky Survey (APASS; Henden et al. 2015).
[e] Strömgren-Crawford *uvbyβ* photometry catalog (Paunzen 2015).
[f] Two-micron All Sky Survey (2MASS; Cutri et al. 2003).
[g] Wide-field Infrared Survey Explorer catalog (WISE; Cutri 2013).

is not sufficient to completely rule out chance alignment with a background source; however, such an alignment with a bright source is highly unlikely. Assuming the *TESS* point-spread function can be approximated by a two-dimensional Gaussian profile with an FWHM of ~25″, we found that 98.9% (98.5%) of the flux from HD 15337 is within the Sector 3 (Sector 4) SPOC aperture. Approximating the *TESS* bandpass with the *Gaia* G_{RP} bandpass, the transit signals from HD 15337 should be diluted by less than 0.01% in both apertures; HD 15337 is the only star bright enough to be the source of the transit signals. Two other *Gaia* DR2 sources (5068777809825770112 and 5068777745400963584) also contribute flux, but they are too faint to yield significant dilution ($G_{RP} \approx 19$ mag). Figure 1
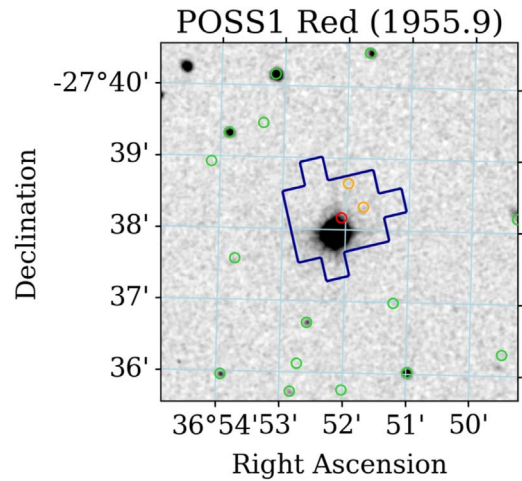

Figure 1. $5' \times 5'$ 103aE emulsion image taken in 1955 from the First Palomar Sky Survey (POSS1-E), with the Sector 4 SPOC photometric aperture overplotted in blue (*TESS* pixel size is 21″), and the positions of *Gaia* DR2 sources (J2015.5) within 2′ of HD 15337 indicated by circles. HD 15337 is in red, nearby sources contributing more than 1% of their flux to the aperture are in orange, and other sources are in green; the Sector 3 aperture is slightly bigger but yields similarly low levels of photometric dilution (see Section 2). Due to the proper motion of HD 15337, there is a ~14″ offset between its *Gaia* position and its position in the image.

shows the archival image, along with *Gaia* DR2 source positions and the Sector 4 SPOC photometric aperture.

3. HARPS Spectroscopic Observations

HD 15337 was observed between 2003 December 15 and 2017 September 6 UT with the HARPS spectrograph ($R \approx 115,000$, Mayor et al. 2003) mounted at the European Southern Observatory (ESO)-3.6 m telescope, as part of the observing programs 072.C-0488, 183.C-0972, 192.C-0852, 196.C-1006, and 198.C-0836. We retrieved the publicly available reduced spectra from the ESO archive, along with the cross-correlation function (CCF) and its bisector, computed from the dedicated HARPS pipeline using a K5 numerical mask (Baranne et al. 1996). On 2015 June, the HARPS fiber bundle was upgraded and a new set of octagonal fibers, with improved mode-scrambling capabilities, were installed (Lo Curto et al. 2015). To account for the RV offset caused by the instrument refurbishment, we treated the HARPS RVs taken before/after 2015 June as two different data sets. Tables 2 and 3 list the HARPS RVs taken with the old and new fiber bundle, along with the RV uncertainties, the FWHM and bisector span (BIS) of the CCF, the exposure times, and the signal-to-noise ratio (S/N) per pixel at 5500 Å. Time stamps are given in barycentric Julian Date in the barycentric dynamical time (BJD_{TDB}). We rejected two data points—marked with asterisks in Tables 2 and 3—because of poor S/N ratio ($BJD_{TDB} = 2455246.519846$) or systematics ($BJD_{TDB} = 2457641.794439$).

4. Stellar Fundamental Parameters

4.1. Spectroscopic Parameters

We co-added the HARPS spectra obtained with the old and new fiber bundle separately to get two combined spectra with S/N per pixel at 5500 Å of 590 (old fiber) and 490 (new fiber). We derived the spectroscopic parameters of HD 15337 from the co-added HARPS spectra using Spectroscopy Made Easy

Table 2
HARPS RV Measurements of HD 15337 Acquired with the Old Fiber Bundle

BJD$_{\rm TDB}$[a] −2450000	RV (km s^{-1})	±σ (km s^{-1})	BIS (km s^{-1})	FWHM (km s^{-1})	$T_{\rm exp}$ (s)	S/N[b]
2988.663700	−3.8208	0.0010	0.0013	6.1330	900	70.8
3270.822311	−3.8260	0.0008	0.0015	6.1353	900	93.7
3785.541537	−3.8234	0.0007	0.0010	6.1471	900	101.7
4422.673842	−3.8155	0.0006	0.0059	6.1571	900	108.1
4424.646720	−3.8111	0.0007	0.0037	6.1531	900	97.7

Notes.
[a] Barycentric Julian dates are given in barycentric dynamical time.
[b] S/N per pixel at 550 nm.
[c] Outlier not included in the analysis.

(This table is available in its entirety in machine-readable form.)

Table 3
HARPS RV Measurements of HD 15337 Acquired with the New Fiber Bundle

BJD$_{\rm TDB}$[a] −2450000	RV (km s^{-1})	±σ (km s^{-1})	BIS (km s^{-1})	FWHM (km s^{-1})	$T_{\rm exp}$ (s)	S/N[b]
7291.826359	−3.7848	0.0008	0.0273	6.2102	900	88.1
7292.799439	−3.7889	0.0007	0.0246	6.2141	900	95.6
7299.843584	−3.7988	0.0007	0.0229	6.1968	900	106.2
7303.879389	−3.7973	0.0013	0.0184	6.1985	900	60.3
7353.698805	−3.7959	0.0008	0.0209	6.2081	900	97.6

Notes.
[a] Barycentric Julian dates are given in barycentric dynamical time.
[b] S/N per pixel at 550 nm.
[c] Outlier not included in the analysis.

(This table is available in its entirety in machine-readable form.)

(SME), a spectral analysis tool that calculates synthetic spectra and fits them to high-resolution observed spectra using a χ^2 minimizing procedure. The analysis was performed with the non-local thermodynamic equilibrium (non-LTE) SME version 5.2.2, along with MARCS model atmospheres (Gustafsson et al. 2008).

We estimated a microturbulent velocity of $v_{\rm mic} = 0.80 \pm 0.10$ km s^{-1} from the empirical calibration equations for Sun-like stars from Bruntt et al. (2010). The effective temperature $T_{\rm eff}$ was measured fitting the wings of the H$_\alpha$ and H$_\beta$ lines, as well as the Na I doublet at 5890 and 5896 Å (Fuhrmann et al. 1993; Axer et al. 1994; Fuhrmann et al. 1994, 1997b, 1997a). The surface gravity log $g_\star$ was determined from the wings of the Ca I λ6102, λ6122, λ6162 Å triplet, and the Ca I λ6439 Å line, as well as from the Mg I λ5167, λ5173, λ5184 Å triplet. We measured the iron abundance [Fe/H], the macroturbulent velocity $v_{\rm mac}$, and the projected rotational velocity $v \sin i_\star$ by simultaneously fitting the unblended iron lines in the spectral region 5880–6600 Å.

Our analyses applied to the two stacked HARPS spectra provided consistent results, well within the uncertainties. The final adopted values are listed in Table 4. We derived an effective temperature of $T_{\rm eff} = 5125 \pm 50$ K, surface gravity log $g_\star = 4.40 \pm 0.10$(cgs), and an iron abundance relative to solar of [Fe/H] = 0.15 ± 0.08 dex. We also measured a calcium abundance of [Ca/H] = 0.16 ± 0.05 dex and a sodium abundance of [Na/H] = 0.27 ± 0.09 dex. We found a macroturbulent velocity of $v_{\rm mac} = 3.0 \pm 1.0$ km s^{-1} in agreement with the value predicted from the empirical

equations of Doyle et al. (2014). The projected rotational velocity was found to be $v \sin i_\star = 1.0 \pm 1.0$ km s^{-1}.

4.2. Stellar Mass, Radius, Age, and Interstellar Extinction

We performed an analysis of the broadband spectral energy distribution (SED) together with the DR2 (Gaia Collaboration et al. 2018) parallax in order to determine an empirical measurement of the stellar radius, following the procedures described in Stassun & Torres (2016), Stassun et al. (2017), and Stassun et al. (2018a). We retrieved the $B_{\rm T}$ and $V_{\rm T}$ magnitudes from Tycho-2 catalog (Høg et al. 2000), the Strömgren ubvy magnitudes from Paunzen (2015), the BVgri magnitudes from APASS (Henden et al. 2015), the JHK$_S$ magnitudes from 2MASS (Cutri et al. 2003), the W1–W4 magnitudes from ALLWISE (Cutri 2013), and the G magnitude from Gaia DR2 (Gaia Collaboration et al. 2018). Together, the available photometry spans the full stellar SED over the wavelength range 0.35–22 μm (Table 1 and Figure 2). In addition, we retrieved the near-ultraviolet (NUV) flux from Galaxy Evolution Explorer (GALEX) survey (Bianchi et al. 2011) in order to assess the level of chromospheric activity, if any.

We performed a fit using Kurucz stellar atmosphere models (Castelli & Kurucz 2003), with the fitted parameters being the effective temperature $T_{\rm eff}$ and iron abundance [Fe/H], as well as the interstellar extinction $A_{\rm v}$, which we restricted to the maximum line-of-sight value from the dust maps of Schlegel et al. (1998). The broadband SED is largely insensitive to the surface gravity (log $g_\star$), thus we simply adopted the value from the initial spectroscopic analysis presented in the previous

Table 4
HD 15337 System Parameters

Parameter	Prior[a]	Derived Value
Stellar Parameters		
Star mass $M_\star$ ($M_\odot$)	...	0.90 ± 0.03
Star radius $R_\star$ ($R_\odot$)	...	0.856 ± 0.017
Effective temperature $T_{\rm eff}$ (K)	...	5125 ± 50
Surface gravity[b] $\log g_\star$ (cgs)	...	4.53 ± 0.02
Surface gravity[c] $\log g_\star$ (cgs)	...	4.40 ± 0.10
Iron abundance [Fe/H] (dex)	...	0.15 ± 0.10
Sodium abundance [Na/H] (dex)	...	0.27 ± 0.09
Calcium abundance [Ca/H] (dex)	...	0.16 ± 0.05
Projected rotational velocity $v \sin i_\star$ (km s^{-1})	...	1.0 ± 1.0
Age (Gyr)	...	5.1 ± 0.8
Interstellar extinction $A_{\rm v}$	...	0.02 ± 0.02
Model Parameters of HD 15337 b		
Orbital period $P_{\rm orb,b}$ (days)	$\mathcal{U}[4.7552, 4.7572]$	4.75615 ± 0.00017
Transit epoch $T_{0,b}$ (BJD$_{\rm TDB}-2\,450\,000$)	$\mathcal{U}[8411.4526, 8411.4706]$	$8411.46156^{+0.00094}_{-0.00119}$
Scaled semimajor axis $a_{\rm b}/R_\star$	$\mathcal{N}[13.11, 0.17]$	$13.11^{+0.16}_{-0.15}$
Planet-to-star radius ratio $R_{\rm b}/R_\star$	$\mathcal{U}[0, 0.1]$	$0.01761^{+0.00055}_{-0.00058}$
Impact parameter $b_{\rm b}$	$\mathcal{U}[0, 1]$	$0.33^{+0.09}_{-0.14}$
$\sqrt{e_{\rm b}} \sin \omega_{\star,{\rm b}}$	$\mathcal{U}[-1, 1]$	$0.22^{+0.09}_{-0.11}$
$\sqrt{e_{\rm b}} \cos \omega_{\star,{\rm b}}$	$\mathcal{U}[-1, 1]$	$0.12^{+0.14}_{-0.18}$
RV semi-amplitude variation $K_{\rm b}$ (m s^{-1})	$\mathcal{U}[0, 10]$	$3.08^{+0.44}_{-0.41}$
Model Parameters of HD 15337 c		
Orbital period $P_{\rm orb,c}$ (days)	$\mathcal{U}[17.1676, 17.1876]$	17.1784 ± 0.0016
Transit epoch $T_{0,c}$ (BJD$_{\rm TDB}-2\,450\,000$)	$\mathcal{U}[8414.5416, 8414.5616]$	8414.5501 ± 0.0015
Scaled semimajor axis $a_{\rm c}/R_\star$	$\mathcal{N}[31.68, 0.70]$	31.87 ± 0.70
Planet-to-star radius ratio $R_{\rm c}/R_\star$	$\mathcal{U}[0, 0.1]$	0.0256 ± 0.0011
Impact parameter $b_{\rm c}$	$\mathcal{U}[0, 1]$	$0.87^{+0.01}_{-0.02}$
$\sqrt{e_{\rm c}} \sin \omega_{\star,{\rm c}}$	$\mathcal{U}[-1, 1]$	$-0.08^{+0.16}_{-0.15}$
$\sqrt{e_{\rm c}} \cos \omega_{\star,{\rm c}}$	$\mathcal{U}[-1, 1]$	$0.12^{+0.15}_{-0.17}$
RV semi-amplitude variation $K_{\rm c}$ (m s^{-1})	$\mathcal{U}[0, 10]$	$2.16^{+0.48}_{-0.45}$
Additional Model Parameters		
Parameterized limb-darkening coefficient q_1	$\mathcal{N}[0.43, 0.1]$	0.37 ± 0.08
Parameterized limb-darkening coefficient q_2	$\mathcal{N}[0.19, 0.1]$	0.25 ± 0.11
Systemic velocity $\gamma_{\rm HS1}$ (km s^{-1})	$\mathcal{U}[-4.0, -3.6]$	-3.8174 ± 0.0027
Systemic velocity $\gamma_{\rm HS2}$ (km s^{-1})	$\mathcal{U}[-4.0, -3.6]$	-3.7977 ± 0.0012
RV jitter term $\sigma_{\rm HS1}$ (m s^{-1})	$\mathcal{U}[0, 100]$	$2.19^{+0.36}_{-0.30}$
RV jitter term $\sigma_{\rm HS2}$ (m s^{-1})	$\mathcal{U}[0, 100]$	$2.89^{+0.58}_{-0.43}$
Stellar rotation period ($P_{\rm rot}$) days	$\mathcal{U}[36.4, 36.6]$	36.528 ± 0.022
Linear RV term m s^{-1} d^{-1}	$\mathcal{U}[-0.1, 0.1]$	-0.0057×0.0017
Quadratic RV term m s^{-1} d^{-1}	$\mathcal{U}[-0.1, 0.1]$	$-13.3 \pm 2.6 \times 10^{-7}$
Derived Parameters of HD 15337 b		
Planet mass $M_{\rm b}$ ($M_\oplus$)	...	$7.51^{+1.09}_{-1.01}$
Planet radius $R_{\rm b}$ ($R_\oplus$)	...	1.64 ± 0.06
Planet mean density $\rho_{\rm b}$ (g cm^{-3})	...	$9.30^{+1.81}_{-1.58}$
Semimajor axis of the planetary orbit $a_{\rm b}$ (au)	...	0.0522 ± 0.0012
Orbit eccentricity $e_{\rm b}$	...	0.09 ± 0.05
Argument of periastron of stellar orbit $\omega_{\star,{\rm b}}$ (deg)	...	62^{+42}_{-32}
Orbit inclination $i_{\rm b}$ (deg)	...	$88.5^{+0.6}_{-0.4}$
Equilibrium temperature [d] $T_{\rm eq,b}$ (K)	...	1001 ± 11.5
Transit duration $\tau_{14,{\rm b}}$ (hr)	...	2.49 ± 0.06
Derived Parameters of HD 15337 c		
Planet mass $M_{\rm c}$ ($M_\oplus$)	...	$8.11^{+1.82}_{-1.69}$
Planet radius $R_{\rm c}$ ($R_\oplus$)	...	2.39 ± 0.12
Planet mean density $\rho_{\rm c}$ (g cm^{-3})	...	$3.23^{+0.90}_{-0.72}$
Semimajor axis of the planetary orbit $a_{\rm c}$ (au)	...	0.1268 ± 0.0038
Orbit eccentricity $e_{\rm c}$	...	$0.05^{+0.06}_{-0.04}$
Argument of periastron of stellar orbit $\omega_{\star,{\rm c}}$ (deg)	...	329^{+69}_{-64}
Orbit inclination $i_{\rm c}$ (deg)	...	$88.5^{+0.2}_{-0.1}$
Equilibrium temperature[d] $T_{\rm eq,c}$ (K)	...	642 ± 10
Transit duration $\tau_{14,{\rm c}}$ (hr)	...	$2.25^{+0.20}_{-0.11}$

Notes.
[a] $\mathcal{U}[a, b]$ refers to uniform priors between a and b; $\mathcal{N}[a, b]$ to Gaussian priors with mean a and standard deviation b.
[b] From spectroscopy and evolutionary tracks.
[c] From spectroscopy.
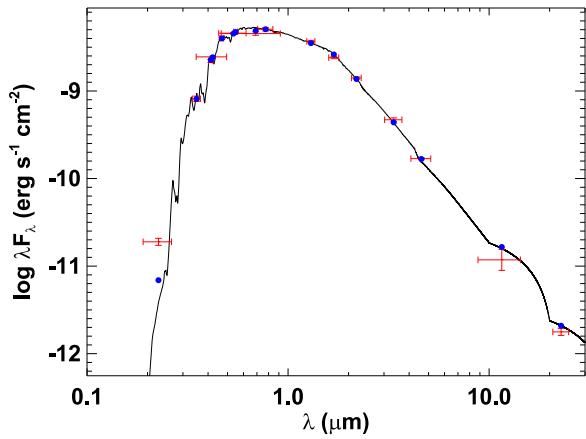[d] Assuming zero albedo and uniform redistribution of heat.

Figure 2. SED of HD 15337. Red symbols represent the observed photometric measurements, where the horizontal bars represent the effective width of the passband. Blue symbols are the model fluxes from the best-fit Kurucz atmosphere model (black).

subsection. The resulting fit (Figure 2) gives a reduced χ^2 of 2.3 (excluding the *GALEX* NUV flux, which is consistent with a modest level of chromospheric activity). The best-fitting effective temperature and iron content are $T_{\rm eff} = 5130 \pm 50$ K and [Fe/H] $= 0.1^{+0.2}_{-0.1}$ dex, respectively, in excellent agreement with the spectroscopic values (Section 4.1 and Table 4). We found that the reddening of HD 15337 is consistent with zero ($A_{\rm v} = 0.02 \pm 0.02$ mag), as expected given the relatively short distance to the star ($\sim$45 pc). Integrating the unreddened model SED gives a bolometric flux at Earth of $F_{\rm bol} = 7.29 \pm 0.08 \times 10^{-9}$ erg s cm^{-2}. Taking the $F_{\rm bol}$ and $T_{\rm eff}$ together with the *Gaia* DR2 parallax, adjusted by $+0.08$ mas to account for the systematic offset reported by Stassun & Torres (2018), gives the stellar radius as $R_\star = 0.856 \pm 0.017 R_\odot$. Finally, estimating the stellar mass from the empirical relations of Torres et al. (2010) and a 6% error from the empirical relation itself gives a stellar mass of $M_\star = 0.91 \pm 0.06 M_\odot$.

We can refine the stellar mass estimate by taking advantage of the observed chromospheric activity, which can constrain the age of the star via empirical relations. For example, taking the chromospheric activity indicator, $\log R'_{\rm HK} = -4.916 \pm 0.038$ from Gomes da Silva et al. (2014) and applying the empirical relations of Mamajek & Hillenbrand (2008), gives a predicted age of 5.1 ± 0.8 Gyr. As shown in Figure 3, according to the Yonsei–Yale stellar evolutionary models (Yi et al. 2001; Spada et al. 2013), this age is most compatible with a stellar mass of $M_\star = 0.90 \pm 0.03 M_\odot$ and [Fe/H] $= 0.25$ dex, which with the empirically determined stellar radius implies a stellar $\log g_\star = 4.53 \pm 0.02$ (cgs). This is in good agreement with the spectroscopic value of $\log g_\star = 4.40 \pm 0.10$ (cgs).

Other combinations of stellar mass and metallicity are compatible with the observed effective temperature and radius (Figure 3); however, they require ages that are incompatible with that predicted by the chromospheric $R'_{\rm HK}$ emission. Finally, we can further corroborate the activity-based age estimate by also using empirical relations to predict the stellar rotation period from the activity. For example, the empirical relation between $R'_{\rm HK}$ and rotation period from Mamajek & Hillenbrand (2008) predicts a rotation period for this star of $\approx$42 days, which is compatible with the observed rotation

period derived from the HARPS RVs and activity indicators ($P_{\rm rot} = 36.5$ days; see the following section).

5. Frequency Analysis of the HARPS Measurements

We performed a frequency analysis of the HARPS time-series to search for the Doppler reflex motion induced by the two transiting planets discovered by *TESS*. We accounted for the RV offset between the two different set-ups of the instrument (old and new fiber bundle) using the value of 19.7 m s^{-1} derived from the joint analysis presented in Section 6, which is in good agreement with the expected offset for a slowly rotating K1 V star such as HD 15337 (Lo Curto et al. 2015).

The offset-corrected HARPS RVs are displayed in Figure 4 (upper panel), along with the time-series of the FWHM (middle panel) and bisector span (BIS; lower panel). The generalized Lomb–Scargle (GLS) periodogram (Zechmeister & Kürster 2009) of the combined RV data shows significant power at frequencies lower than the inverse of the temporal baseline of the HARPS observations, which is visible as a quadratic trend in the upper panel of Figure 4. A similar trend is observed in the FWHM obtained with the old fiber bundle (middle panel, blue circles), suggesting that the RV trend might be due to long-term stellar variability (e.g., magnetic cycles).[41] Alternatively, the RV trend might be induced by a long period orbiting companion, while the long-term variation of the FWHM might be ascribable to the steady instrument de-focusing observed between 2004 and 2015 (Lo Curto et al. 2015).

The upper panel of Figure 5 shows the GLS periodogram of the combined HARPS RVs, following the subtraction of the best-fitting quadratic trend (cfr. Figure 4). The peaks with the highest power are found at the orbital frequencies of the two transiting planets ($f_c = 0.058$ c/d and $f_b = 0.210$ c/d), with false-alarm probabilities[42] (FAPs) of $\approx$1% and RV semi-amplitude of about 2.0–2.5 m s^{-1}. The periodogram of the RV residuals after subtracting the signal of the outer planet (Figure 5, second panel), shows a significant peak (FAP < 0.1%) at the frequency of the inner planet. The two peaks have no counterparts in the periodograms of the activity indicators[43] (FWHM and BIS; Figure 5, fourth and fifth panels), suggesting that the signals are induced by two orbiting planets with periods of 4.8 and 17.2 days. Finally, the GLS periodogram of the RV residuals after subtracting the quadratic trend and the signals of the two planets (Figure 5, third panel) displays a peak with a FAP < 0.1% at $\sim$36.5 days, which is also significantly detected in the periodogram of the FWHM (fourth panel). We interpreted the 36.5 days signal as the rotation period of the star, which agrees with the value expected from the $R'_{\rm HK}$ activity indicator (Section 4.2).

6. Joint Analysis

We performed a joint analysis of the *TESS* light curve (Section 2) and RV measurements (Section 3) using the software suite pyaneti, which allows for parameter

---

[41] We note that the FWHM and BIS offsets between the two instrument set-ups are unknown.
[42] The FAP was derived using the bootstrap method described in (Kuerster et al. 1997).
[43] We combined the activity indicators from the two HARPS fibers by subtracting the best-fitting second-order polynomials shown in Figure 4.
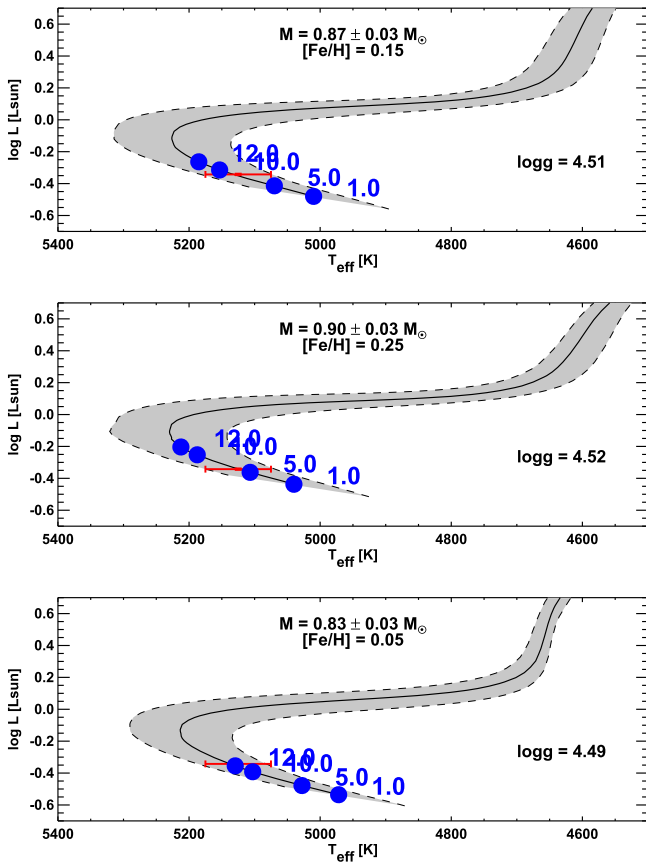
Figure 3. Hertzsprung–Russell Diagram for HD 15337 based on the observed effective temperature and bolometric luminosity, the latter computed directly from F_{bol} and the *Gaia* parallax-based distance. Each panel compares the observed properties of the star to evolutionary tracks from the Yonsei–Yale models (Yi et al. 2001; Spada et al. 2013) for different permitted combinations of stellar mass and metallicity. Blue points with labels represent the model ages in Gyr. The central panel represents the case most compatible with all of the available data, including the stellar age of $\approx$5.1 Gyr as determined from the observed chromospheric activity and stellar rotation period (see the text).
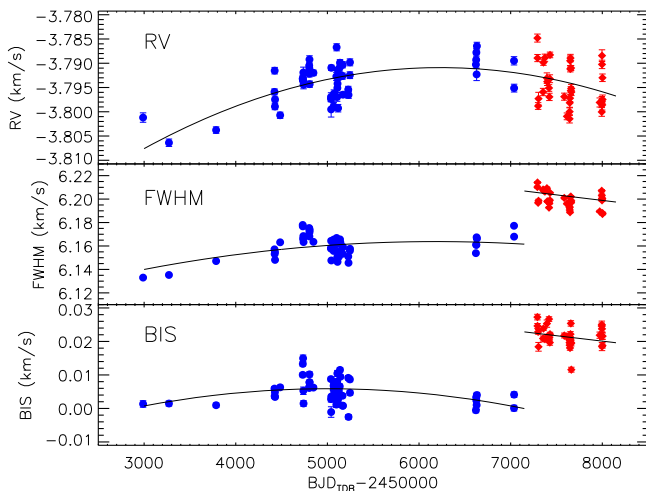
Figure 4. Offset-corrected HARPS RVs of HD 15337 (upper panel), and FWHM and BIS of the cross-correlation function (middle and lower panels). The blue circles and red diamonds mark the measurements acquired with the old and new fiber bundle, respectively. The thick lines mark the best-fitting parabolic curves to the data (see the text).

estimation from posterior distributions calculated using Markov chain Monte Carlo (MCMC) methods.

We removed stellar variability from the *TESS* light curves using a cubic spline with knots spaced every 1.5 days. We then extracted ~8 hours of *TESS* photometry centered on each of the nine (HD 15337 b) and three (HD 15337 c) transits observed by *TESS* during Sectors 3 and 4. As described in Section 3, we rejected two HARPS RVs and used the remaining 85 Doppler measurements, while accounting for an RV offset between the two different HARPS set-ups.

The RV model includes a linear and a quadratic term, to account for the long-term variation described in Section 5, as well as two Keplerians, to account for the Doppler reflex motion induced by HD 15337 b and HD 15337 c. The RV stellar signal at the star's rotation period was modeled as an additional coherent sine-like curve whose period was constrained with a uniform prior centered at $P_{rot} = 36.5$ days and having a width of 0.2 days, as derived from the FWHM of the peak detected in the periodogram of the HARPS FWHMs. For the phase and amplitude of the activity signal we adopted uniform priors. While this simple model might not fully reproduce the periodic and quasi-periodic variations induced by evolving active regions carried around by stellar rotation, it has proven to be effective in accounting for the stellar signal of active and moderately active stars (e.g., Pepe et al. 2013; Gandolfi et al. 2017; Barragán et al. 2018; Prieto-Arranz et al. 2018). Any variation not properly modeled by the coherent sine-curve, and/or any instrumental noise not included in the nominal RV uncertainties, were accounted for by fitting two RV jitter terms for the two HARPS set-ups.

We modeled the *TESS* transit light curves using the limb-darkened quadratic model of Mandel & Agol (2002). For the limb-darkening coefficients, we set Gaussian priors using the values derived by Claret (2017) for the *TESS* passband. We imposed conservative error bars of 0.1 on both the linear and quadratic limb-darkening terms. For the eccentricity and argument of periastron we adopted the parametrization proposed by Anderson et al. (2011). A preliminary analysis showed that the transit light curve poorly constrains the scaled semimajor axis ($a/R_\star$). We therefore set a Gaussian prior on $a/R_\star$ using *Kepler*'s third law, the orbital period, and the derived stellar mass and radius (Section 4.2). We imposed uniform priors for the remaining fitted parameters. Details of the fitted parameters and prior ranges are given in Table 4. We used 500 independent Markov chains initialized randomly inside the prior ranges. Once all chains converged, we used the last 5000 iterations and saved the chain states every 10 iterations. This approach generates a posterior distribution of 250,000 points for each fitted parameter. Table 4 lists the inferred planetary parameters. They are defined as the median and 68% region of the credible interval of the posterior distributions for each fitted parameter. The transit and RV curves are shown in Figure 6 and Figure 7, along with the best-fitting models.

We also experimented with Gaussian Processes (GPs) to model the correlated RV noise associated with stellar activity. GPs model stochastic processes with a parametric description of the covariance matrix. GP regression has proven to be successful in modeling the effect of stellar activity for several other exoplanetary systems (see, e.g., Haywood et al. 2014; Grunblatt et al. 2015; López-Morales et al. 2016;
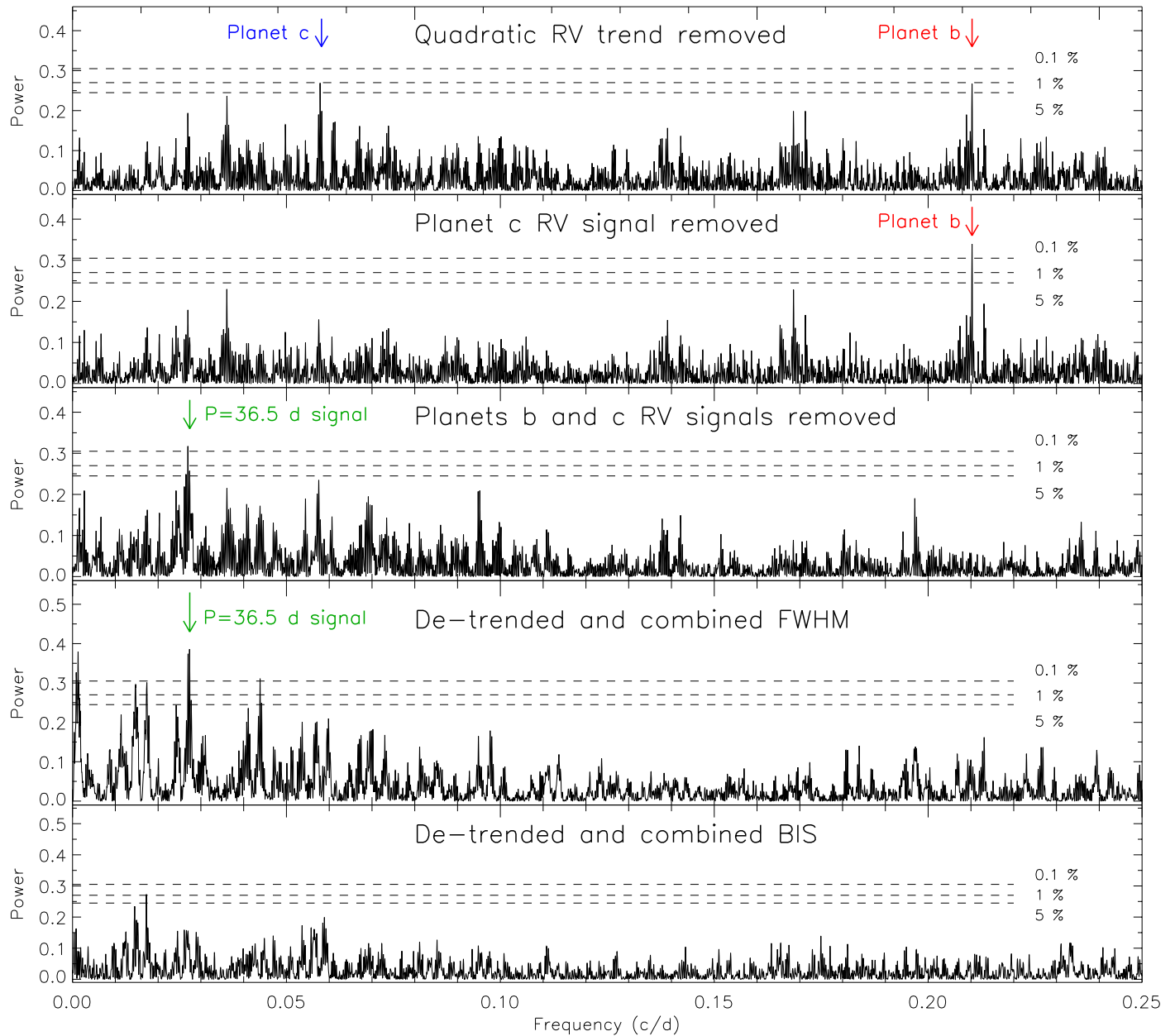
Figure 5. GLS periodograms of (1) the combined HARPS RV measurements, following the subtraction of the quadratic trend (first panel); (2) the RV residuals after subtracting the signal of HD 15337 c (second panel); (3) the RV residuals after subtracting the signal of HD 15337 b and c (third panel); (4) the FWHM of the cross-correlation function (fourth panel); (5) the bisector span (BIS) of the cross-correlation function (fifth panel). The dashed horizontal lines mark the FAP at 0.1%, 1% and 5%. The frequencies of the two transiting planets, as well as of the signal at 36.5 days, are marked with vertical arrows.

Barragán et al. 2018). To this aim, we modified the code `pyaneti` in order to include a GP algorithm coupled to the MCMC method. We implemented the GP approach proposed by Rajpaul et al. (2015). Briefly, this framework assumes that the star-induced RV variations and activity indicators can be modeled by the same underlying GP and its derivative. This allows the GP to disentangle the RV activity component from the planetary signals.

We assumed that the stellar activity can be modeled by the quasi-periodic kernel described by Rajpaul et al. (2015). We modeled together the HARPS RV, BIS, and FWHM time-series and we treated RV and BIS as being described by the GP and its first derivative, while for FWHM we assumed that it is only described by the GP. The fitted hyper-parameters are then V_c, V_r, B_c, B_r, L_c, as defined by Rajpaul et al. (2015), to account

for the GP amplitudes of the RV, BIS, and FWHM signals, the period of the activity signal P_{GP}, the inverse of the harmonic complexity λ_p, and the long term evolution timescale λ_e. We coupled this GP approach with the joint modeling described in the previous paragraphs of the present section (omitting the extra coherent signal).

As for the planetary signals, we imposed the same priors listed in Table 4. For the hyper-parameters, we used uniform priors, except for P_{GP}, for which we imposed a Gaussian prior with mean 36.5 days and standard deviation of 0.2 day. We used 250 chains to explore the parameter space. We created the posterior distributions with 500 iterations of converged chains, which generated a posterior distribution with 250,000 points for each parameters.
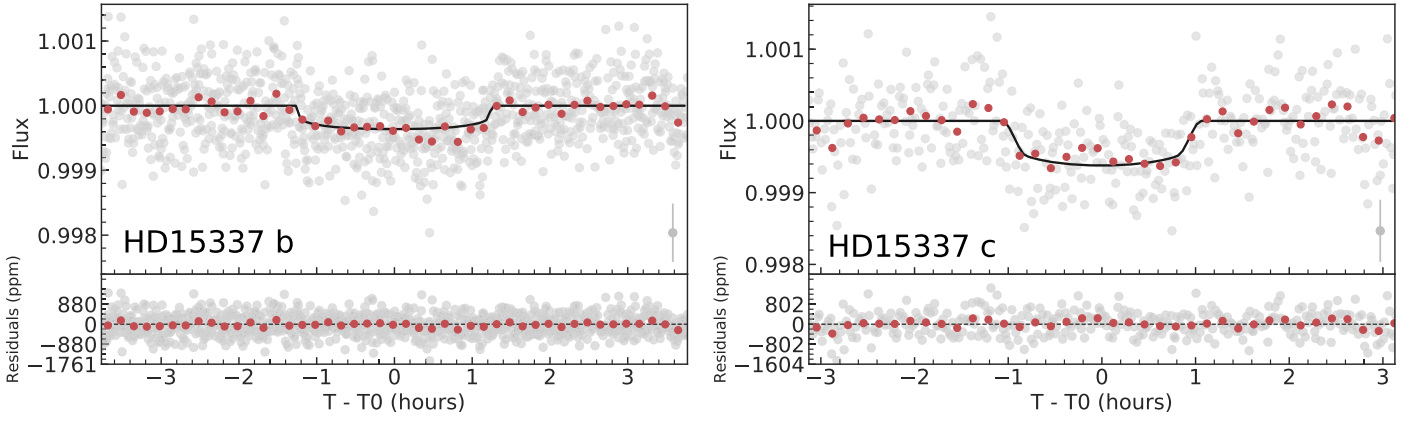
Figure 6. Folded transit light curves of HD 15337 b (left panel) and HD 15337 c (middle panel), based on nine and three single transits observed by *TESS*. The best-fitting transit models are overplotted with thick black lines. The *TESS* data points are shown with gray circles, whereas the 10 minutes binned data are displayed with red circles.
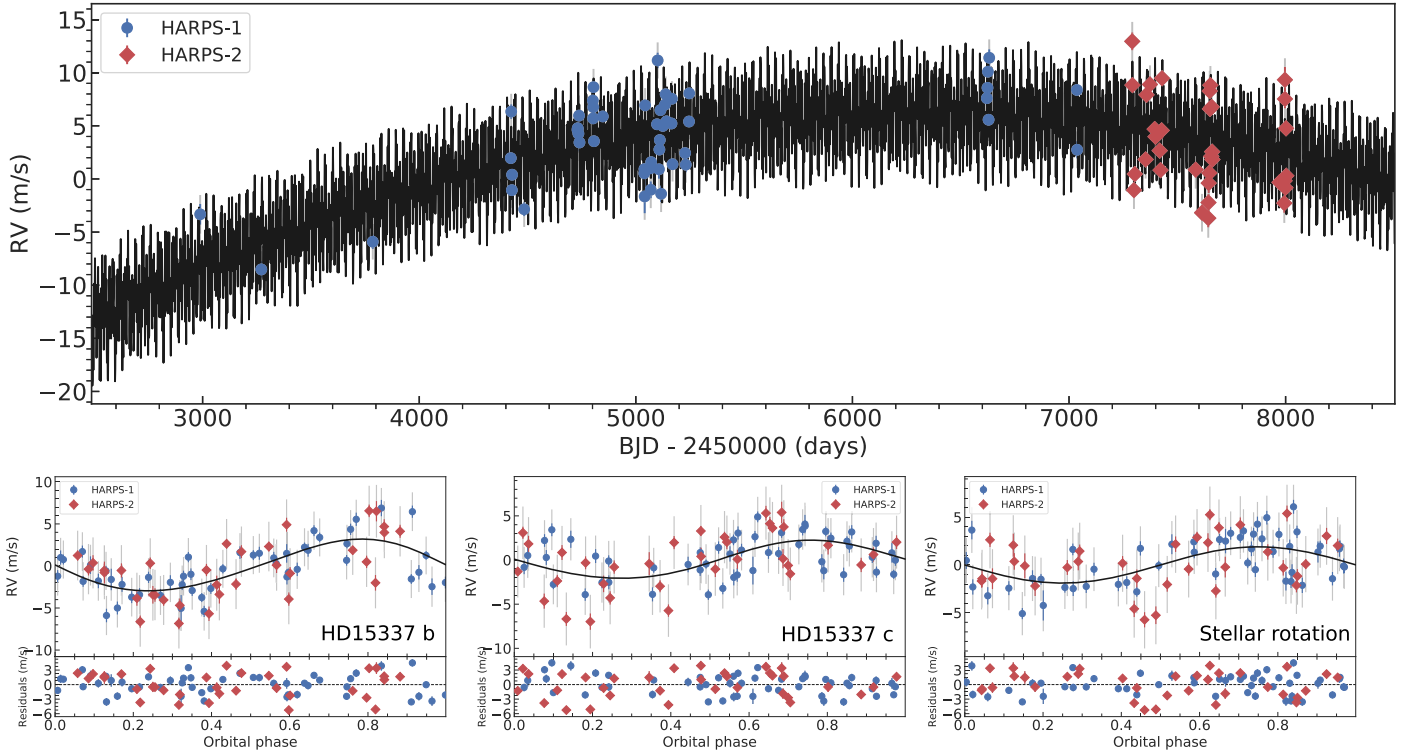

Figure 7. Upper panel: HARPS RV measurements vs. time, following the subtraction of the systemic velocities derived for the old (blue circles) and new (red diamonds) instrument set-up. Lower panels: phase-folded RV curves of HD 15337 b (left), HD 15337 c (middle) and stellar signal at 36.5 days (right). The best-fitting Keplerian and sine models are overplotted with thick black lines. The vertical gray lines mark the error bars including the RV jitter.

For planets b and c we derived an RV semi-amplitude of $2.71^{+0.54}_{-0.51}$ m s^{-1} and $2.06^{+0.64}_{-0.58}$ m s^{-1}, respectively, which are in very good agreement with the values reported in Table 4. The other planetary and orbital parameters are also consistent with the values presented in Table 4. For the GP hyper-parameters, we found $V_c = 0.55 \pm 0.23$ m s^{-1}, $V_r = 70^{+27}_{-21}$ m s^{-1}, $B_c = 9.4^{+3.4}_{-2.9}$ m s^{-1}, $B_r = 64^{+20}_{-25}$ m s^{-1}, $L_c = 5.4 \pm 2.2$ m s^{-1} $P_{GP} = 36.5 \pm 0.2$ d, $\lambda_e = 4217^{+624}_{-685}$ d, and $\lambda_p = 1086^{+501}_{-394}$. The relatively large values of the scale parameters in the GP, i.e., λ_e and λ_p, indicate that the stellar activity behaves like a sinusoidal signal (with slight corrections).

7. Discussion and Conclusions

The innermost transiting planet HD 15337 b ($P_{orb,b} = 4.8$ days) has a mass of $M_b = 7.51^{+1.09}_{-1.01}$ $M_\oplus$ and a radius of $R_b = 1.64 \pm 0.06$ $R_\oplus$, yielding a mean density of $\rho_b = 9.30^{+1.81}_{-1.58}$ g cm^{-3}. Figure 8 displays the position of HD 15337 b on the mass–radius diagram compared to the sub-sample of small transiting planets ($R_p \leqslant 3 R_\oplus$) whose masses and radii have been derived with a precision better than 25%. Theoretical models from Zeng et al. (2016) are overplotted using different lines and colors. Given the precision of our mass determination (∼14%), we
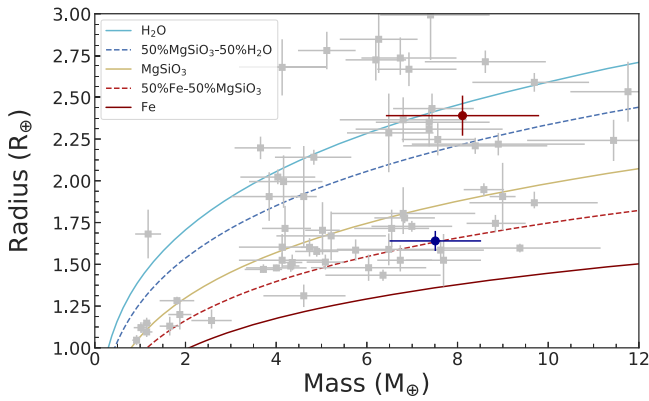
Figure 8. Mass–radius diagram for low-mass ($M_p < 12\ M_\oplus$), small ($R_p < 3\ R_\oplus$) planets with mass–radius measurements better than 25% (from http://www.astro.keele.ac.uk/jkt/tepcat/; Southworth 2011). Composition models from Zeng et al. (2016) are displayed with different lines and colors. The solid blue and red circles mark the position of HD 15337 b and HD 15337 c, respectively.

conclude that HD 15337 b is a rocky terrestrial planet with a composition consisting of ∼50% silicate and ∼50% iron.

For HD 15337 c ($P_{orb,c} = 17.2$ days), we obtained a mass of $M_c = 8.11^{+1.82}_{-1.69}\ M_\oplus$ and a radius of $R_c = 2.39 \pm 0.12\ R_\oplus$, yielding a mean density of $\rho_c = 3.23^{+0.90}_{-0.72}$ g cm^{-3}. Therefore, HD 15337 b and c have similar masses, but the radius of HD 15337 c is ∼1.5 times larger than the radius of HD 15337 b. The lower bulk density of HD 15337 c suggests that the planet is likely composed by a rocky core surrounded either by a considerable amount of water, or by a light, hydrogen-dominated envelope. In the case of a water-rich planet, the amount of water and high planetary equilibrium temperature would imply the presence of a steam atmosphere, which would be strongly hydrogen dominated in its upper layer, as a consequence of water dissociation and the low mass of hydrogen. It is therefore plausible to assume that HD 15337 c hosts a hydrogen-dominated atmosphere, at least in its upper part.

As in other systems hosting two close-in sub-Neptune-mass planets (e.g., HD 3167 Gandolfi et al. 2017), the radii of HD 15337 b and c lie on opposite sides of the radius gap (Fulton et al. 2017; Van Eylen et al. 2018), with the closer-in planet having a higher bulk density, similar to other close-in systems with measured planetary masses (e.g., HD 3167, K2-109, GJ 9827; Gandolfi et al. 2017; Guenther et al. 2017; Prieto-Arranz et al. 2018). This gap is believed to be caused by atmospheric escape (Owen & Wu 2017; Jin & Mordasini 2018), which is stronger for closer-in planets. Within this picture, HD 15337 b would probably have lost its primary, hydrogen-dominated atmosphere and now hosts a secondary atmosphere possibly resulting from out-gassing of a solidifying magma ocean, while HD 15337 c is likely to still partly retain the primordial hydrogen-dominated envelope. This is consistent with Van Eylen et al. (2018), who measured the location and slope of the radius gap as a function of orbital period and matched it to models suggesting a homogeneous terrestrial core composition.

To first order, the radii of HD 15337 b and c depend on the present-day properties of their atmospheres, which are intimately related to the amount of high-energy (X-ray and extreme ultraviolet; $\lambda < 91.2$ nm) stellar radiation received since the dispersal of the protoplanetary nebula, and thus also
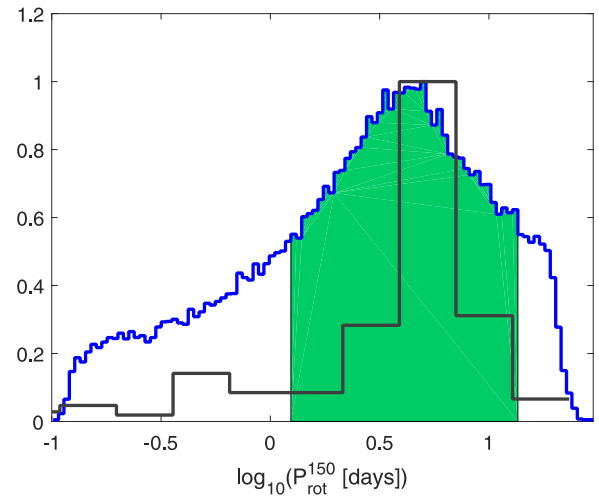

Figure 9. MCMC posterior distributions for the stellar rotation period at an age of 150 Myr obtained from the modeling of HD 15337 c. The shaded areas correspond to the 68% region of the credible interval of the posterior distribution. The black histogram shows the distribution of stellar rotation periods measured for open cluster stars with an age of 150 Myr (from Johnstone et al. 2015).

to the stellar rotation history. The evolution of the stellar rotation rate does not follow a unique path because stars of the same mass and metallicity can have significantly different rotation rates up to about 1 Gyr (e.g., Mamajek & Hillenbrand 2008; Johnstone et al. 2015; Tu et al. 2015). For older stars, it is therefore not possible to infer their past high-energy emission from their measured stellar properties. Starting from the assumption that HD 15337 c hosted a hydrogen-dominated atmosphere with solar metallicity throughout its entire evolution, we derived the history of the stellar rotation and high-energy emission by modeling the atmospheric evolution of HD 15337 c. To this end, we employed the atmospheric evolution algorithm described by Kubyshkina et al. (2018) and further developed by Kubyshkina et al. (2019), which is based on a Bayesian approach, fitting the currently observed planetary radius and combining the planetary evolution model with the MCMC open-source algorithm of Cubillos et al. (2017). The planetary atmospheric evolution model, system parameters (i.e., planetary mass, planetary radius, orbital separation, current stellar rotation period, stellar age, stellar mass; Table 4) were then used to compute the posterior distribution for the stellar rotation rate at any given age via MCMC. We assumed Gaussian priors determined by the measured system parameters and their uncertainties.

Figure 9 shows the obtained posterior distribution for the rotation period HD 15337 at an age of 150 Myr in comparison with the distribution derived from measurements of open cluster stars of the same age (Johnstone et al. 2015). Our results indicate that HD 15337, when it was young, was likely to be a moderate rotator, with a high-energy emission at 150 Myr ranging between 3.7 and 127 times the current solar emission, further excluding that the star was a very fast/slow rotator. We further employed the result shown in Figure 9 to estimate the past atmospheric evolution of a possible hydrogen-dominated atmosphere of HD 15337 b. Accounting for all uncertainties on the system parameters and on the derived history of the stellar rotation period, we obtained that HD 15337 b has completely lost its primary atmosphere, assuming it held one, within

300 Myr, in agreement with the currently observed mean density.

The position of HD 15337 c in the mass–radius diagram (Figure 8) indicates that the planet may be hosting a massive hydrogen-dominated envelope or a smaller secondary atmosphere. As primary atmospheres are easily subject to escape, knowing the current composition of the envelope of HD 15337 c would provide a strong constraint on atmospheric evolution models. In this respect, this planet is similar to π Men c (Gandolfi et al. 2018; Huang et al. 2018); furthermore, as for π Men, the close distance to the system and brightness of the host star would enable high-quality transmission spectroscopy spanning from far-ultraviolet to infrared wavelengths. Of particular interest would be probes of an extended, escaping atmosphere. Spectral lines sensitive to various levels of extended atmospheres include H I, C II, and O I resonance lines in the ultraviolet, H_α in the optical, and He I in the near-infrared. This suite of lines would provide a comprehensive picture of the upper atmosphere of the planet, thus constraining atmospheric escape and evolution models.

Facilities: TESS, HARPS.

Software: VARLET (Grziwa & Pätzold 2016), PHALET (Grziwa & Pätzold 2016), SME (Valenti & Piskunov 1996; Valenti & Fischer 2005; Piskunov & Valenti 2017), pyaneti (Barragán et al. 2019).

ORCID iDs

Davide Gandolfi ⓘ https://orcid.org/0000-0001-8627-9628
Luca Fossati ⓘ https://orcid.org/0000-0003-4426-9530
John H. Livingston ⓘ https://orcid.org/0000-0002-4881-3620
Keivan G. Stassun ⓘ https://orcid.org/0000-0002-3481-9052
Sascha Grziwa ⓘ https://orcid.org/0000-0003-3370-4058
Malcolm Fridlund ⓘ https://orcid.org/0000-0003-2180-9936
Daria Kubyshkina ⓘ https://orcid.org/0000-0001-9137-9818
Juan Cabrera ⓘ https://orcid.org/0000-0001-6653-5487
William D. Cochran ⓘ https://orcid.org/0000-0001-9662-3496
Hans J. Deeg ⓘ https://orcid.org/0000-0003-0047-4241
Michael Endl ⓘ https://orcid.org/0000-0002-7714-6310
Teruyuki Hirano ⓘ https://orcid.org/0000-0003-3618-7535
Petr Kabath ⓘ https://orcid.org/0000-0002-1623-5352
Norio Narita ⓘ https://orcid.org/0000-0001-8511-2981
Prajwal Niraula ⓘ https://orcid.org/0000-0002-8052-3893
Grzegorz Nowak ⓘ https://orcid.org/0000-0002-7031-7754
Seth Redfield ⓘ https://orcid.org/0000-0003-3786-3486
Ignasi Ribas ⓘ https://orcid.org/0000-0002-6689-0312
Marek Skarka ⓘ https://orcid.org/0000-0002-7602-0046

References

Alibert, Y., & Benz, W. 2017, A&A, 598, L5
Alibert, Y., Mousis, O., Mordasini, C., & Benz, W. 2005, ApJL, 626, L57
Anderson, D. R., Collier Cameron, A., Hellier, C., et al. 2011, ApJL, 726, L19
Axer, M., Fuhrmann, K., & Gehren, T. 1994, A&A, 291, 895
Baranne, A., Queloz, D., Mayor, M., et al. 1996, A&AS, 119, 373
Barragán, O., Gandolfi, D., & Antoniciello, G. 2019, MNRAS, 482, 1017
Barragán, O., Gandolfi, D., Dai, F., et al. 2018, A&A, 612, A95
Bianchi, L., Herald, J., & Efremova, B. 2011, Ap&SS, 335, 161
Bruntt, H., Bedding, T. R., Quirion, P.-O., et al. 2010, MNRAS, 405, 1907
Castelli, F., & Kurucz, R. L. 2003, in IAU Symp. 210, Modelling of Stellar Atmospheres, ed. N. Piskunov, W. W. Weiss, & D. F. Gray (San Francisco, CA: ASP), A20
Christiansen, J. L., Jenkins, J. M., Caldwell, D. A., et al. 2012, PASP, 124, 1279
Claret, A. 2017, A&A, 600, A30
Cubillos, P., Harrington, J., Loredo, T. J., et al. 2017, AJ, 153, 3
Cutri, R. M. 2013, yCat, 2328
Cutri, R. M., Skrutskie, M. F., van Dyk, S., et al. 2003, yCat, 2246
Doyle, A. P., Davies, G. R., Smalley, B., Chaplin, W. J., & Elsworth, Y. 2014, MNRAS, 444, 3592
Esposito, M., Armstrong, D. J., Gandolfi, D., et al. 2019, A&A, 623, A165
Fuhrmann, K., Axer, M., & Gehren, T. 1993, A&A, 271, 451
Fuhrmann, K., Axer, M., & Gehren, T. 1994, A&A, 285, 585
Fuhrmann, K., Pfeiffer, M., Frank, C., Reetz, J., & Gehren, T. 1997a, A&A, 323, 909
Fuhrmann, K., Pfeiffer, M. J., & Bernkopf, J. 1997b, A&A, 326, 1081
Fulton, B. J., Petigura, E. A., Howard, A. W., et al. 2017, AJ, 154, 109
Gaia Collaboration, Brown, A. G. A., Vallenari, A., et al. 2018, A&A, 616, A1
Gandolfi, D., Barragán, O., Hatzes, A. P., et al. 2017, AJ, 154, 123
Gandolfi, D., Barragán, O., Livingston, J. H., et al. 2018, A&A, 619, L10
Gomes da Silva, J., Santos, N. C., Boisse, I., Dumusque, X., & Lovis, C. 2014, A&A, 566, A66
Grunblatt, S. K., Howard, A. W., & Haywood, R. D. 2015, ApJ, 808, 127
Grziwa, S., & Pätzold, M. 2016, arXiv:1607.08417
Guenther, E. W., Barragán, O., Dai, F., et al. 2017, A&A, 608, A93
Gustafsson, B., Edvardsson, B., Eriksson, K., et al. 2008, A&A, 486, 951

Haywood, R. D., Collier Cameron, A., Queloz, D., et al. 2014, MNRAS, 443, 2517
Henden, A. A., Levine, S., Terrell, D., & Welch, D. L. 2015, AAS Meeting, 225, 336.16
Høg, E., Fabricius, C., Makarov, V. V., et al. 2000, A&A, 355, L27
Huang, C. X., Burt, J., Vanderburg, A., et al. 2018, ApJL, 868, L39
Jenkins, J. M., Twicken, J. D., McCauliff, S., et al. 2016, Proc. SPIE, 9913, 99133E
Jin, S., & Mordasini, C. 2018, ApJ, 853, 163
Johnstone, C. P., Güdel, M., Brott, I., & Lüftinger, T. 2015, A&A, 577, A28
Jones, M. I., Brahm, R., Espinoza, N., et al. 2018, A&A, in press (arXiv:1811. 05518)
Kovács, G., Zucker, S., & Mazeh, T. 2002, A&A, 391, 369
Kubyshkina, D., Cubillos, P. E., Fossati, L., et al. 2019, ApJ, in press
Kubyshkina, D., Fossati, L., Erkaev, N. V., et al. 2018, A&A, 619, A151
Kuerster, M., Schmitt, J. H. M. M., Cutispoto, G., & Dennerl, K. 1997, A&A, 320, 831
Lo Curto, G., Pepe, F., Avila, G., et al. 2015, Msngr, 162, 9
López-Morales, M., Haywood, R. D., Coughlin, J. L., et al. 2016, AJ, 152, 204
Mamajek, E. E., & Hillenbrand, L. A. 2008, ApJ, 687, 1264
Mandel, K., & Agol, E. 2002, ApJL, 580, L171
Mayor, M., Pepe, F., Queloz, D., et al. 2003, Msngr, 114, 20
Nielsen, L. D., Bouchy, F., Turner, O., et al. 2019, A&A, 623, A100
Owen, J. E., & Wu, Y. 2017, ApJ, 847, 29
Paunzen, E. 2015, A&A, 580, A23
Pepe, F., Cameron, A. C., Latham, D. W., et al. 2013, Natur, 503, 377
Piskunov, N., & Valenti, J. A. 2017, A&A, 597, A16
Prieto-Arranz, J., Palle, E., Gandolfi, D., et al. 2018, A&A, 618, A116
Quinn, S. N., Becker, J. C., Rodriguez, J. E., et al. 2019, arXiv:1901.09092
Rajpaul, V., Aigrain, S., Osborne, M. A., Reece, S., & Roberts, S. 2015, MNRAS, 452, 2269
Ricker, G. R., Winn, J. N., Vanderspek, R., et al. 2015, JATIS, 1, 014003
Schlegel, D. J., Finkbeiner, D. P., & Davis, M. 1998, ApJ, 500, 525
Smith, J. C., Stumpe, M. C., Van Cleve, J. E., et al. 2012, PASP, 124, 1000
Southworth, J. 2011, MNRAS, 417, 2166
Spada, F., Demarque, P., Kim, Y.-C., & Sills, A. 2013, ApJ, 776, 87
Stassun, K. G., Collins, K. A., & Gaudi, B. S. 2017, AJ, 153, 136
Stassun, K. G., Corsaro, E., Pepper, J. A., & Gaudi, B. S. 2018a, AJ, 155, 22
Stassun, K. G., Oelkers, R. J., Pepper, J., et al. 2018b, AJ, 156, 102
Stassun, K. G., & Torres, G. 2016, AJ, 152, 180
Stassun, K. G., & Torres, G. 2018, ApJ, 862, 61
Stumpe, M. C., Smith, J. C., Van Cleve, J. E., et al. 2012, PASP, 124, 985
Torres, G., Andersen, J., & Giménez, A. 2010, A&A Rev., 18, 67
Trifonov, T., Rybizki, J., & Kürster, M. 2019, A&A, 622, L7
Tu, L., Johnstone, C. P., Güdel, M., & Lammer, H. 2015, A&A, 577, L3
Valenti, J. A., & Fischer, D. A. 2005, ApJS, 159, 141
Valenti, J. A., & Piskunov, N. 1996, A&AS, 118, 595
Van Eylen, V., Agentoft, C., Lundkvist, M. S., et al. 2018, MNRAS, 479, 4786
Yi, S., Demarque, P., Kim, Y.-C., et al. 2001, ApJS, 136, 417
Zechmeister, M., & Kürster, M. 2009, A&A, 496, 577
Zeng, L., Sasselov, D. D., & Jacobsen, S. B. 2016, ApJ, 819, 127